Dalton Transactions

ROYAL SOCIETY OF CHEMISTRY

PAPER

View Article Online
View Journal | View Issue

Cite this: *Dalton Trans.*, 2025, **54**, 11868

Construction of Ni^{3+}-rich, Ru-doped NiO nanoparticles with lattice strain for enhanced OER performance†

Yi Wang,[a] Yu Zhang,[a] Jingce Bi,[a] Huichun Xue,[b] Ningning Liu,[c] Jie Sun,[a] Xia Zhang,[a] Zhuopeng Wang,[a] Lin Zhu[b] and Yide Han*[a]

Received 30th April 2025,
Accepted 7th July 2025

DOI: 10.1039/d5dt01013f

rsc.li/dalton

Manipulating the intrinsic activity of heterogeneous catalysts at the atomic level is an effective strategy to improve their electrocatalytic performances but remains a great challenge. Herein, we synthesized Ni^{3+}-rich, Ru-doped NiO nanoparticles (Ru–NiO) through a two-step thermal treatment method. As an OER catalyst, the obtained Ru–NiO exhibited a low overpotential of 220 mV at a current density of 10 mA cm^{-2} and a Tafel slope of 78 mV dec^{-1} in alkaline media, outperforming NiO-based electrocatalysts prepared *via* the conventional sol–gel synthesis method and conventional calcination synthesis method. Employing this strategy, the introduction of trace amounts of Ru atoms in the NiO lattice, leading to lattice strain and electron redistribution, results in superior OER activity. Our results further illustrate that the Ru–O–Ni bonds in the precursor play a vital role in this strategy for the formation of Ru–NiO nanoparticles with lattice strain. At the same time, density functional theory (DFT) results further confirmed that the Ru–NiO nanoparticles have a low d-band center caused by the lattice strain effect to improve the adsorption energy of oxygen-containing intermediates, ultimately accelerating OER kinetics. Thus, this work provides a new pathway for the design of NiO-based OER catalysts.

1. Introduction

Electrocatalytic water splitting is regarded as a promising approach for H_2 production and reducing fossil fuel energy consumption.[1] Electrocatalytic water splitting consists of two half-reactions: the cathodic hydrogen evolution reaction (HER) and anodic oxygen evolution reaction (OER).[2,3] Currently, the bottleneck in this process is mainly derived from the complicated multi-step proton-coupled electron transfer in the anodic OER,[4] which results in a high kinetic barrier and low electrolysis efficiency, consequently requiring a large overpotential to overcome its sluggish reaction kinetics.[5] Therefore, intensive efforts have been devoted to developing well-known state-of-the-art noble metal Ir- and Pt-based catalysts for the OER.[6,7] Nevertheless, their high cost, scant reserves and instability largely prevent their practical applications.[8,9] Consequently, considerable attempts have been devoted to developing relatively cost-effective and earth-abundant alternatives to these electrocatalysts.

Recently, transition metal oxides as OER electrocatalysts have aroused increasing attention owing to their abundant reserves, low lost and comparable catalytic activities to noble metals.[10] Among them, NiO possessing excellent redox reversibility, a large surface area and high activity has been applied to catalyze the OER in the electrocatalytic water splitting process.[11] However, the OER performance of pristine NiO is still insufficient to meet the industrial demand because of its undesirable electrical conductivity, inferior stability and limited number of active sites.[12] As a consequence, developing versatile strategies to precisely modulate the electronic configuration of NiO is crucial, thereby enhancing its active site density while optimizing its adsorption/desorption energetics for reactants and intermediates, which could ultimately lead to significantly improved oxygen evolution reaction (OER) catalytic performance.

Recently, lattice-strain engineering to improve electrocatalytic performance by regulating electron configuration has become a hotspot in the field of the OER.[13–15] Many types of strain strategies have been reported to achieve unique catalytic activity. Among them, heterogeneous atom doping is a promising strategy. Moreover, it has been proven that doping high-valent non-3d transition metal ions can effectively adjust the electronic structure of 3d metals and increase the number of

[a]*Department of Chemistry, College of Sciences, Northeastern University, Shenyang, 110819, P. R. China. E-mail: hanyide@mail.neu.edu.cn*
[b]*Department of Physics, College of Sciences, Northeastern University, Shenyang, 110819, P. R. China*
[c]*School of Petrochemical Engineering, Liaoning Petrochemical University, Fushun, Liaoning 113001, P. R. China*

†Electronic supplementary information (ESI) available. See DOI: https://doi.org/10.1039/d5dt01013f

active sites, thus enhancing their electrochemical performance.[16] As a typical high-valent non-3d transition metal ion, the ionic radius of Ru^{3+} (0.68 Å) is similar to that of Ni^{2+} (0.69 Å), which makes the entry of Ru into the NiO lattice possible. Furthermore, the electronegativity value of Ru^{3+} is larger than that of Ni^{2+}, which can adjust the electronic structure of NiO when Ru atom is doped into the NiO lattice.[17] Consequently, it can be inferred that doping the Ru atom into the NiO lattice can efficiently induce lattice strain and accurately regulate its electronic structure, simultaneously boosting the valence state of Ni species to improve its catalytic OER performance. However, both the conventional sol–gel method and the conventional calcination method can induce phase changes during the introduction of the Ru atom into the NiO lattice, further inhibiting the formation of the Ru–O–Ni bond in the intermediate, which eventually leads to the difficult entry of Ru atoms into the NiO lattice matrix.

Herein, we synthesized Ni^{3+}-rich, Ru-doped NiO nanoparticles (Ru–NiO) through a two-step thermal treatment method, which showed a superior performance in the oxygen evolution reaction (OER) compared with the catalysts prepared *via* the conventional sol–gel synthesis method and conventional calcination synthesis method. The incorporation of Ru atoms induced a lattice-strain effect, leading to electron redistribution and an increase in high-valent Ni^{3+} active sites, which consequently enhanced its oxygen evolution reaction (OER) performance. This was proven by density functional theory (DFT) calculation results. Simultaneously, during the two-step thermal treatment process, the appropriate pretreatment temperature (160 °C) was found to be crucial for introducing the Ru atom into the NiO lattice. Our results further confirmed the advantage of the two-step thermal treatment strategy for the introduction of the Ru atom into NiO lattice.

2. Experimental section

2.1. Materials and reagents

$Ni(NO)_2{\cdot}6H_2O$, ethylene glycol (EG), triethanolamine (TEOA), and $RuCl_3{\cdot}xH_2O$ were purchased from Tianjin Tianli Chemical Reagent Co., Ltd, Sinopharm Chemical Reagent Co., Ltd, Tianjin kemiou Chemical Reagent Co., Ltd, and Shanghai Macklin Biochemical Co., Ltd, respectively. Ethylene glycol was used to prepare all samples. All reagents were analytical grade reagents and used without further purification.

2.2. Preparation of pure Ni and 3% Ru-doped Ni sol precursor solutions

6.9790 g (24 mmol) of nickel nitrate hexahydrate $Ni(NO_3)_2{\cdot}6H_2O$ and 3.2 mL of triethanolamine were dissolved in 22.5 mL of ethylene glycol (C_2H_6O). Then, 7.5 mL of ethylene glycol solution containing a concentration of 0.096 M Ru^{3+} was added to the above-mentioned mixed solution. The mixed solution was stirred for 2 h at 80 °C and aged for 24 h at room temperature to form the 3% Ru-doped Ni sol precursor solutions. Meanwhile, Ni sol precursor solutions without Ru doping were prepared in the same way as mentioned above.

2.3. Preparation of precursor wet gel and Ru–NiO-*T* and NiO

The 3% Ru-doped sol precursor solution was pretreated at different temperatures (120 °C, 160 °C, 190 °C, 200 °C, 250 °C and 270 °C, respectively) for 3 h at a rate of 1 °C min^{-1} in air to form a wet gel. Subsequently, the obtained wet gel was calcined at 450 °C for 4 h at a rate of 5 °C min^{-1} in air to generate Ru–NiO-*T* nanoparticles (*T* stands for precursor pretreatment temperature, and the sample named Ru–NiO when *T* = 160 °C). As a comparison, pristine NiO nanoparticles without Ru doping were also synthesized using the above-mentioned method (named NiO).

2.4. Preparation of Ru–NiO-1 and Ru–NiO-2

Two samples were synthesized *via* the conventional sol–gel method[18] and conventional calcination method,[19] respectively. 3% Ru-doped Ni sol precursor solutions were heated to form a dry gel, and the resultant dry gel was ground and calcined at 450 °C for 4 h at a heating rate of 5 °C min^{-1} to form the reference sample (named Ru–NiO-1). In addition, a 3% Ru-doped Ni sol–gel precursor solution was directly calcined at 450 °C for 4 h at a heating rate of 5 °C min^{-1} to form the reference sample *via* the conventional calcination method (named Ru–NiO-2).

2.5. Electrochemical measurement

All electrochemical tests were performed on a Shanghai Chenhua 660E workstation. The electrocatalytic water oxidation activity of the samples were measured using the typical three-electrode system with Pt and Hg/HgO as the counter and reference electrodes, respectively. In this work, all the potentials were referenced to the reversible hydrogen electrode (RHE). The OER performance of the obtained samples was evaluated by coating them on functionalized exfoliated graphite foil (FEG) electrodes.[20] All samples were tested in 1 M KOH electrolyte. The method for preparing the electrode was as follows: the as-prepared samples, PVDF and conductive carbon black in a ratio of 7 : 2 : 1 were mixed and ground, and then *N*-methyl-2-pyrrolidone (NMP) was added to form a slurry. Afterwards, the slurry was coated on the FEG (1 × 1 cm^2), and then the obtained FEG was dried at 80 °C for 8 h. The catalyst loading was approximately 1 mg cm^{-2}.

2.6. Physical characterization

Powder X-ray diffraction patterns (PXRD) were recorded using a Rigaku D/max 2500 diffractometer with Cu Kα radiation. The morphology and structure of the catalysts were observed by scanning electron microscopy (SEM, Hitachi S4800) and high-resolution transmission electron microscopy (HR-TEM, Talos F200X) equipped with an energy dispersive X-ray spectroscopy (EDX) detector. The FTIR spectra of the samples were recorded in transmission mode (Thermo Nicolet 8700 FTIR) in the range of 4000–400 cm^{-1}. X-ray photoelectron spectroscopy (XPS) (PerkinElmer PHI5300) was performed to analyze the surface compositions and valence state of the elements.

3. Characterization

3.1. Exploration of optimal synthesis methods

According to Scheme 1, the synthesis of 3% Ru-doped NiO nanoparticle (Ru–NiO) was achieved through a two-step thermal treatment method. Briefly, a 3% Ru-doped Ni sol–gel precursor solution was prepared utilizing ethylene glycol as the solvent and TEOA as a chelating agent and surfactant. Subsequently, the obtained sol–gel precursor was heated at 160 °C, and then calcinated in air at 450 °C. As shown in Fig. 1a, the diffraction peaks of all the samples at 37.4°, 43.44°, 62.98°, 75.58° and 79.52° can be assigned to the (111), (200), (220), (311) and (222) planes of NiO (JCPDS no. 04-0835), respectively. This result indicates that no phase change occurred when Ru was doped in the NiO lattice. However, it was found that the diffraction peaks of all the Ru-doped NiO samples slightly shifted towards the high angle region, which can be attributed to the lattice-strain due to the substitution of Ru for Ni in the NiO lattice.[21] Among the three samples, the biggest peak shift was observed for Ru–NiO, which indicates that using two-step thermal treatment strategy to introduce the Ru atom in the NiO lattice is a highly effective method. According to Bragg's equation, the greater the diffraction peak shift to the high angle area, the smaller the lattice parameter, indicating a certain degree of lattice compression compared to pristine NiO. Thus, it was found that the lattice parameter of Ru–NiO is smaller than that of the pristine NiO, which was further supported by DFT calculations (Table S1†). The Ru–NiO, Ru–NiO-1 and Ru–NiO-2 catalysts were analyzed by Fourier transform infrared spectroscopy (FTIR). As shown in Fig. 1b, a sharp absorption peak near 470 cm^{-1} was observed for the three samples, which belongs to the Ni–O bond. Excitingly, an additional peak appeared at 570 cm^{-1} in the FTIR spectrum of Ru–NiO, which belongs to the Ru–O–Ni bonding vibration.[22,23] This indicates that the Ru atom can react with lattice oxygen to form Ru–O–Ni bonds *via* the two-step thermal treatment strategy. However, no peak corresponding to the Ru–O–Ni bond was found in the spectrum of Ru–NiO-1. Meanwhile, a strong peak attributed to the Ru–O bond at 580 cm^{-1} is clearly observed in the spectrum of Ru–NiO-2, which may be due to the formation of RuO_2 by the conventional calcination method. On account of the abovementioned analysis, we believe that using the two-step thermal treatment method is more conducive to the entry of the Ru atom into the NiO lattice.

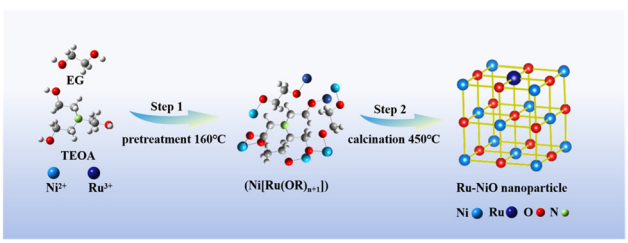

Scheme 1 Synthesis of 3% Ru-doped NiO nanoparticles achieved through a two-step thermal treatment method.

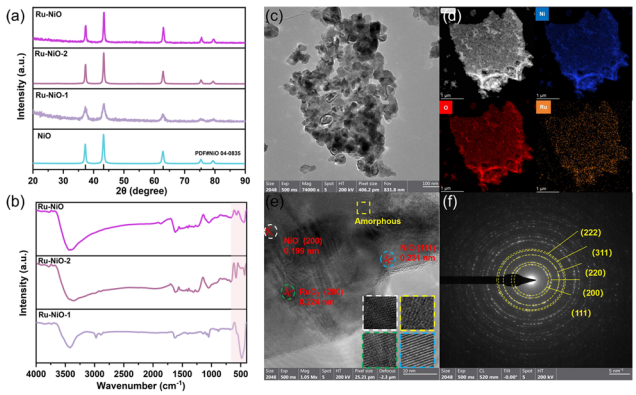

Fig. 1 Morphological and structural characterization. (a) XRD patterns of Ru–NiO, Ru–NiO-2, Ru–NiO-1, NiO and simulated data from the reported crystal structure. (b) FTIR spectra of Ru–NiO, Ru–NiO-2, and Ru–NiO-1. (c) TEM image of Ru–NiO. (d) Corresponding elemental EDX mapping of Ru–NiO. (e) HRTEM image of Ru–NiO; (f) SAED pattern of the Ru–NiO nanoparticles.

Scanning electron microscopy (SEM) and transmission electron microscopy (TEM) revealed that the as-prepared Ru–NiO is composed of near-spherical nanoparticles with a diameter of about 25 nm (Fig. 1c and Fig. S1†). The corresponding elemental mapping by energy dispersive X-ray (EDX) spectroscopy demonstrated that Ru, Ni, and O elements are uniformly distributed on the surface of the Ru–NiO nanoparticles (Fig. 1d). This serves as evidence for the formation of a uniform Ru-doped NiO structure in the nanoparticles without phase segregation. The high-resolution TEM (HRTEM) image of the Ru–NiO nanoparticles provided clear microstructural information about the Ru–NiO interface. As shown in Fig. 1e, two distinct lattice stripes with the measured interplanar crystal spacings of 0.231 nm and 0.199 nm can be observed, corresponding to the (111) and (200) crystal planes of NiO, respectively. Interestingly, these two interplanar crystal spacings of Ru–NiO are smaller than that of the pristine NiO (111 and 0.241 nm) and (200 and 0.208 nm), which could be caused by the lattice strain due to the incorporation of the Ru atom into the NiO lattice. Additionally, one lattice stripe spacing is 0.224 nm, which belongs to the crystal plane of RuO_2 (200). Briefly, the lattice positions of the Ni atoms were replaced by Ru atoms in the Ru–NiO sample, resulting in lattice distortion and a reduction in the interplanar spacing. The results demonstrate that Ru–NiO exhibits a certain degree of lattice compression in comparison to the pristine NiO, which is consistent with the above-mentioned results of the XRD analysis. Therefore, the decrease in the lattice parameter confirms the successful doping of the Ru atom in the NiO lattice. In addition, oxygen vacancies were formed as the substitution reaction occurred, consistent with the results reported in other references.[24] As shown in Fig. 1e, an amorphous region can be clearly observed in the Ru–NiO sample, which is caused by

oxygen vacancies. This can lead to the generation of dislocation defects and unsaturated coordinated sites, which can optimize the local electronic structure and increase the access to the active sites, eventually improving the electrocatalytic activity.[25] Furthermore, the selected area electron diffraction (SAED) pattern indicates that the Ru–NiO nanoparticles have high crystallinity (Fig. 1f). It is worth noting that SAED revealed the (111), (200), (220), (311) and (222) crystal planes of the NiO nanoparticles, which are in accordance with the results of the XRD analysis. Nevertheless, no Ru species was found in the SAED pattern, which further suggests that a trace amount of Ru atoms substituted the Ni atoms in the NiO lattice. The XRD and HRTEM results substantiate that the doping of the Ru^{3+} cation into the NiO matrix led to a lattice strain effect.

To study the electronic structure information of the samples, X-ray photoelectron spectroscopy (XPS) was carried out. The XPS survey spectrum of Ru–NiO confirms the presence of Ni, Ru, C, O, and N (Fig. S2a†), indicating the formation of Ru–NiO (the corrected C 1s binding energy was calculated to be 284.80 eV, and all spectral peaks were adjusted accordingly). The high-resolution XPS Ni $2p_{3/2}$ spectra of Ru–NiO, pristine NiO, Ru–NiO-1 and Ru–NiO-2 are shown in Fig. 2a and Fig. S2b.† It can be seen that the Ni $2p_{3/2}$ XPS curve of Ru–NiO is obviously different from that of the pristine NiO, Ru–NiO-1 and Ru–NiO-2. Two main peaks are centered at 854.28 eV and 856.10 eV, which are assigned to Ni^{2+} and Ni^{3+}, respectively.[26,27] Among these samples, the Ni^{3+}/Ni^{2+} ratio in the Ru–NiO nanoparticles is highest, suggesting the existence of rich Ni^{3+} species on their surface. Moreover, the electronegativity of the Ni atom (Pauling electronegativity of 1.91) is lower than that of Ru atom (Pauling electronegativity of 2.20), indicating that the electrons can be withdrawn from the Ni atom to the Ru atom *via* Ru–O–Ni bonding in the Ru–NiO nanoparticles.[28] Meanwhile, it is worth noting that the binding energy of Ni $2p_{3/2}$ in the Ru–NiO nanoparticles exhibits a positive shift by about 0.3 eV, 0.3 eV and 0.5 eV compared with that of Ru–NiO-1 and Ru–NiO-2, and NiO (Table S2†), respectively. These results imply that the Ru atom in the place of Ni atom in the NiO lattice is conducive to the formation of rich Ni^{3+} species on the surface of the Ru–NiO nanoparticles. It is well known that the high valence state NiOOH species are the real active sites for the OER. For example, we reported the construction of Ni^{3+}-rich nanograss arrays through the introduction of the high-valence metal strategy. The result indicates that the Ni^{3+}-rich system can facilitate the formation of NiOOH species, leading to an improvement in the OER performance.[16] Moreover, increasing the Ni^{3+}/Ni^{2+} ratio in NiO nanoparticles is a great challenge. In this case, the Ni^{3+}/Ni^{2+} ratio in the Ru–NiO nanoparticles was improved enormously compared to the pristine NiO, Ru–NiO-1 and Ru–NiO-2 (Table S3†). Thus, it can be concluded that the *in situ* substitution of the Ni atom by the Ru atom in the NiO lattice favors the regulation of the electronic configuration of the Ni atoms and increases the Ni^{3+}/Ni^{2+} ratio, which is beneficial for the enhancement of the real active sites and the OER catalytic activity. As seen in Fig. 2b, the high-resolution O 1s spectrum of Ru–NiO shows the characteristic peaks at 528.50 eV, 529.56 eV, 531.17 eV and 533.02 eV, which are attributed to the metal–oxygen M–O (Ru–O or Ni–O) bond,[29] OH bond[30] and oxygen vacancy (O_v) bond[31] and CO_3^{2-}, respectively.[32] Compared to the binding energy of O 1s for the pristine NiO, Ru–NiO-1 and Ru–NiO-2 samples, a significant negative shift in this peak can be observed for the Ru–NiO nanoparticles. This means that the electron deflection occurs between Ni and O (Fig. 2b, Fig. S2 and Table S2†). In addition, the peak area of lattice O in the NiO lattice became smaller, while that of oxygen vacancies became larger, suggesting the formation of more oxygen vacancies when the Ru atom is introduced into the NiO lattice. However, there was no obvious change in the peak area of the oxygen vacancies and lattice oxygen in the Ru–NiO-1 and Ru–NiO-2 samples (Fig. 2b). To further illustrate this phenomenon, the formation energy of O vacancies for the pristine NiO and Ru–NiO samples was calculated using the DFT+U method (Table S6†). The results demonstrate that it is very easy to form O vacancies in the NiO lattice upon doping the Ru atom. As seen in Fig. S2d,† the binding energy of Ru $3p_{3/2}$ is located at 463.16 eV in Ru–NiO, 463.98 eV in Ru–NiO-1 and 463.89 eV in Ru–NiO-2. This indicates that the valence state of Ru is +4 in these samples.[33] It can be seen that the binding energy of Ru in Ru–NiO undergoes a more significant negative shift compared to that of Ru–NiO-1 and Ru–NiO-2, which manifests that the two-step thermal treatment method makes it easier for the Ru atom to enter the NiO lattice, and while more electrons could be withdrawn from the Ni atom through the Ru–O–Ni bonding in the Ru–NiO nanoparticles. The results of the Bader charge calculation revealed that the sectional charge of the Ni atom adjacent to the Ru atom in the Ru–NiO nanoparticles decreases from 1.2 to 1.16, which is consistent with the DFT+U calculation and XPS results. According to the Bader charge analysis, it can be observed that the charge around the Ni atom decreases, while that around the Ru atom increases, indicating that electron transfer occurs

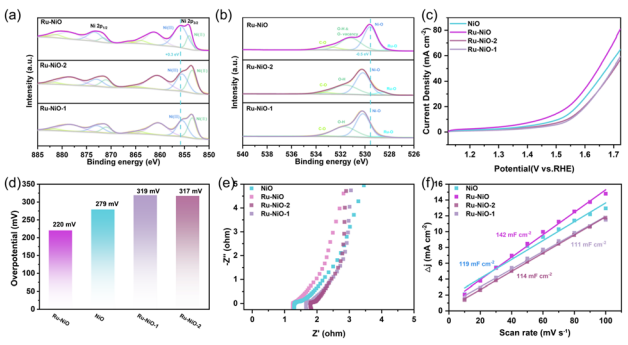

Fig. 2 (a and b) High-resolution Ni 2p, O 1s XPS spectra of Ru–NiO, Ru–NiO-2 and Ru–NiO-1; (c) polarization curves; (d) corresponding overpotential at 10 mA cm^{-2} (η_{10}); (e) Nyquist plots of Ru–NiO, NiO, Ru–NiO-1 and Ru–NiO-2 recorded at a potential of 1.53 V (*vs.* RHE); (f) plots used to calculate surface double-layer capacitance (C_{dl}) of Ru–NiO, NiO, Ru–NiO-1 and Ru–NiO-2.

from the Ni atom to the Ru atom by O bridges in Ru–NiO. Thus, these results elucidate that the lattice strain effect facilitates local reconstruction or mutation of the atomic and electronic configurations on the catalyst surface.[34] Furthermore, it also demonstrates that the two-step thermal treatment strategy could achieve more Ru atoms in the place of Ni atoms in the NiO lattice and modulate the electronic structure of the Ni atom as well as increase the Ni^{3+}/Ni^{2+} ratio, ultimately generating high valence state NiOOH species as the active sites for the OER.

To evaluate the OER performance, electrochemical tests were carried out for Ru–NiO, pristine NiO, Ru–NiO-1 and Ru–NiO-2. The linear scanning voltammetry curves are shown in Fig. 2c, where it can be observed that the catalytic activity of Ru–NiO is better than that of pristine NiO, Ru–NiO-1 and Ru–NiO-2. Fig. 2d shows the corresponding overpotentials @10 mA cm^{-2} (η_{10}) for Ru–NiO, pristine NiO, Ru–NiO-1 and Ru–NiO-2. Among them, the Ru–NiO nanoparticles exhibit the lowest overpotential of 220 mV at the current density of 10 mA cm^{-2}, which is significantly superior to that of NiO (279 mV), Ru–NiO-1 (319 mV), and Ru–NiO-2 (317 mV), indicating that the *in situ* substitution of the Ni atom by the Ru atom in the NiO lattice is beneficial for the OER. Fig. S3† presents the corresponding Tafel slopes of 102 mV dec^{-1}, 78 mV dec^{-1}, 147 mV dec^{-1}, and 146 mV dec^{-1} for the pristine NiO, Ru–NiO, Ru–NiO-1, and Ru–NiO-2, respectively, further revealing that the Ru–NiO nanoparticles exhibit excellent reaction kinetics. Additionally, the electrocatalytic activity of Ru–NiO is superior to several reported NiO-based electrocatalysts and homemade RuO_2 (Table S7 and Fig. S4†). To further probe the charge transfer processes, electrochemical impedance spectroscopy (EIS) was performed. As shown in Fig. 2e, among these samples, Ru–NiO displays the smallest radius, demonstrating that it possesses the lowest charge transfer resistance (R_{ct}) and the best electrical conductivity. The electrochemical active surface area (ECSA) of the samples was assessed by measuring their double-layer capacitance (C_{dl}). The C_{dl} was calculated based on the cyclic voltammograms (CVs) at different scan rates to understand the source of the remarkable OER activity (Fig. S5a–d†). The C_{dl} value of the Ru–NiO nanoparticles is the highest, 142 mF cm^{-2}, surpassing that of the pristine NiO, Ru–NiO-1 and Ru–NiO-2 nanoparticles. This result indicates that the Ru–NiO nanoparticles possess the maximum ECSA and more exposed active sites for electrochemical activity (Fig. 2f). The enhanced OER activity of the Ru–NiO nanoparticles is attributed to their abundance of Ni^{3+} active sites by introducing the Ru atom into the NiO lattice. Furthermore, the faradaic efficiency was tested to determine whether the current density was mainly derived from O_2 evolution. As shown in Fig. S6a,† the high faradaic efficiency (about 76%) of the Ru–NiO nanoparticles confirms their highly efficient current-to-oxygen conversion. Additionally, long-term stability is another essential criterion for evaluating the practical application of catalysts. Remarkably, the Ru–NiO nanoparticles showed favorable operating OER stability with no significant potential change at 10 mA cm^{-2} over 24 h (Fig. S6b†). Besides, they displayed considerable durability during the chronopotentiometric stability test (Fig. S6c†). It is obvious that the current density of the Ru–NiO nanoparticles remained around 99%, suggesting their great stability for OER. Fig. S6d† exhibits the multi-step chronopotentiometric curve for the Ru–NiO nanoparticles in 1 M KOH at current densities ranging from 20 mA cm^{-2} to 240 mA cm^{-2} without the *iR* correction. The potential leveled off at 1.56 V for the initial current value and remained unchanged for 500 s. This result implies that the Ru–NiO nanoparticles can facilitate the rapid outward release of oxygen gas and inward diffusion of the electrolyte, suggesting effective mass transportation behavior.[35] In short, doping the Ru atom into the NiO lattice can reduce the overpotential and increase the ECSA, which are beneficial for the structural stability of the Ru–NiO nanoparticles and the release of oxygen bubbles. It can be inferred that using the two-step thermal treatment strategy is more conducive to the substitution of Ru for Ni in the NiO lattice, resulting in more catalytically active sites of Ni^{3+} for OER.

3.2. Effect of two-step thermal treatment on entry of Ru into NiO lattice

A series of samples was synthesized under different pretreatment temperature conditions (120 °C, 160 °C, and 190 °C) to investigate the effect of temperature on the incorporation of Ru into the NiO crystal lattice. As shown in Fig. 3a, the characteristic peaks of NiO (JCPDS no. 04-0835) were observed in all the samples, which shifted to the higher angle area, indicating the presence of lattice distortion caused by the introduction of Ru into the NiO lattice. However, the extra diffraction peaks of metal Ni^0 (JCPDS no. 01-0126) can be observed in Ru–NiO-190, which is due to the reduction of metal ions in the presence of EG under high-temperature conditions.[36] Additionally, the diffraction peak intensity of metal Ni^0 increased gradually as

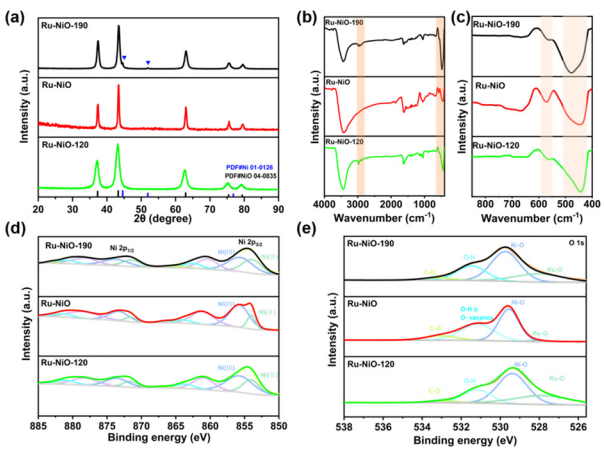

Fig. 3 (a) XRD patterns of Ru–NiO, Ru–NiO-120, and Ru–NiO-190 and simulated data from the reported crystal structure; (b) FTIR spectra of Ru–NiO, Ru–NiO-120 and Ru–NiO-190; (c) localized magnification of the FTIR spectra of Ru–NiO, Ru–NiO-120 and Ru–NiO-190; (d and e) high-resolution Ni 2p and O 1s XPS spectra of Ru–NiO, Ru–NiO-120 and Ru–NiO-190.

the precursor treatment temperature increased (Fig. S9a†). This is because the reduction capacity of EG increases with an increase in the precursor treatment temperature, resulting in more Ni^{2+} being reduced to metal Ni^0 in the sample.[37,38]

Fig. 3b shows the FTIR spectra of Ru–NiO-120, Ru–NiO and Ru–NiO-190. A peak corresponding to the C–H bond can be observed at 2850–3000 cm^{-1} in the spectra of Ru–NiO-120 and Ru–NiO-190, which is similar to that of Ru–NiO-1 and Ru–NiO-2 (Fig. 2b). This result is attributed to the residual alkyl group in the M–O–R bond of the metal alcoholate (M represents a metal ion, while R represents an alkyl group). Conversely, the disappearance of the C–H bonds in the Ru–NiO samples may be ascribed to the fact that the double metal association reaction is more likely to occur at 160 °C, resulting in the formation of intermediate $Ni[Ru(OR)_{n+1}]$, which makes the removal of C–H bonds easier after annealing treatment. Therefore, this intermediate is more favorable to form an Ni–O–Ru bond.[39,40] However, it can be found that Ru–NiO showed the characteristic peak at 470 cm^{-1} (Ni–O bond), which is broad with a weak intensity, while it has a stronger characteristic peak at 570 cm^{-1} compared to Ru–NiO-120 and Ru–NiO-190, resulting from the existence of the Ru–O–Ni bond derived from the pretreated precursors at 160 °C (Fig. 3c). This result indicates that the two-step thermal treatment strategy can enhance the entry of the Ru atom into the NiO lattice because it provides suitable conditions for the association reaction of bimetallic alcohol salts, but this process needs to be carried out within a specific temperature range.

The FTIR spectra of all the precursors were recorded to further explore the influence of temperature on the association reaction process. As shown in Fig. S7a and S7b,† peaks corresponding to the C–H bond (2850–3000 cm^{-1}) can be observed for all the samples, which are attributed to M–O–R (Ni/Ru–O–R and $Ni[Ru(OR)_{n+1}]$) or polyhydric alcohols (EG or TEOA). The peaks at 3000–3500 cm^{-1} belong to the OH group of EG or TEOA.[41] With an increase in the pretreatment temperature (120–190 °C), the intensity of the peaks corresponding to the OH and C–H bonds decreased due to the increase in the degree of deprotonation and the evaporation of EG and TEOA, respectively.[42,43] Combined with the XRD analysis results (Fig. S9a†), Ni^{2+} was reduced to metal Ni^0 when the pretreatment temperature increased to 190 °C, while low a deprotonation degree occurred when the temperature was 120 °C. These results are disadvantageous for the formation of Ni/Ru–O–R or $Ni[Ru(OR)_{n+1}]$, and unfavorable for the creation of Ru–O–Ni bonds, ultimately restricting the entry of the Ru atom into the NiO lattice. In summary, an appropriate pretreatment temperature (160 °C) not only offers proper conditions for the association reaction of bimetallic alcoholates, but also avoids the phase change caused by the reduction of polyhydric alcohol and helps to form Ru–O–Ni bonds and promote the entry of the Ru atom into the NiO lattice.

XPS was performed to investigate the effects of the pretreatment conditions on the electronic structure of Ru–NiO-120, Ru–NiO and Ru–NiO-190. The high-resolution Ni $2p_{3/2}$ spectrum is shown in Fig. 3d, where it can be seen that the binding energy of Ni $2p_{3/2}$ in Ru–NiO is positively shifted compared with that of Ru–NiO-120 and Ru–NiO-190 (Table S4†). This result further implies that the proper pretreatment temperature (160 °C) is more favorable for the substitution of the Ru atom for the Ni atom in the NiO lattice. Meanwhile, the highest Ni^{3+}/Ni^{2+} ratio was also found in Ru–NiO, meaning that the introduction of Ru atoms can further regulate the electronic structure and create more catalytically active sites (Table S5†). Interestingly, the Ni^{3+}/Ni^{2+} ratio in the samples synthesized *via* the two-step thermal treatment method is higher than that synthesized by the conventional sol–gel method and conventional calcination method (Fig. 2a and Table S3†). This indicates that the two-step thermal treatment method is more effective than the traditional methods in promoting the entry of the Ru atom into the NiO lattice. The high-resolution O 1s spectra of Ru–NiO-120, Ru–NiO and Ru–NiO-190 are shown in Fig. 3e. In the case of Ru–NiO, more oxygen vacancies are formed due to the introduction of more Ru atoms into the NiO lattice, according to the peak area ratio of lattice oxygen and oxygen vacancy. However, this phenomenon is not obvious in Ru–NiO-120 and Ru–NiO-190. In addition, it can be seen that the peak intensity of Ru–O in Ru–NiO is lower than that in Ru–NiO-120 and Ru–NiO-190, demonstrating that it is more favorable for the Ru atom to enter the NiO lattice when the pretreatment temperature is 160 °C. This result is also confirmed by the fact that the intensity of Ru 3p in Ru–NiO is the lowest compared with Ru–NiO-120 and Ru–NiO-190 (Fig. S6b†). Thus, the XPS results show that the two-step thermal treatment method is more beneficial for the entry of the Ru atom into the NiO lattice, and the optimization of the electronic structure is more obvious when the pretreatment temperature is 160 °C (with the highest Ni^{3+}/Ni^{2+} ratio).

The linear scanning voltammetry curves of Ru–NiO-120, Ru–NiO and Ru–NiO-190 are shown in Fig. 4a. As seen in Fig. 4b, Ru–NiO exhibits the lowest overpotential of 220 mV at the current density of 10 mA cm^{-2}, making it superior to Ru–NiO-120 (239 mV) and Ru–NiO-190 (252 mV). As shown in Fig. S8a,† Ru–NiO shows the lowest Tafel slope value, demonstrating its enhanced OER kinetics. In addition, Ru–NiO shows the best electron conductivity (Fig. 4c and d) and the largest number of electroactive sites (Fig. S8b–d†) for OER tests. Furthermore, Fig. S9(b–d)† show the electrochemical properties of the samples treated at higher precursor treatment temperatures (Ru–NiO-200, Ru–NiO-250 and Ru–NiO-270), which deteriorated compared with that of Ru–NiO-160. This implies that the appropriate pretreatment temperature (160 °C) is more favorable for the substitution of Ru for Ni in the NiO lattice, further regulating the electronic structure and create more catalytically active sites. It is interesting that the electrochemical properties of the sample synthesized *via* the two-step thermal treatment method are superior to that of the samples synthesized *via* the conventional sol–gel method and conventional calcination method (Fig. 2c–f). This indicates that the two-step thermal treatment method is more effective than the traditional methods in promoting the entry of the Ru atom into the NiO lattice.

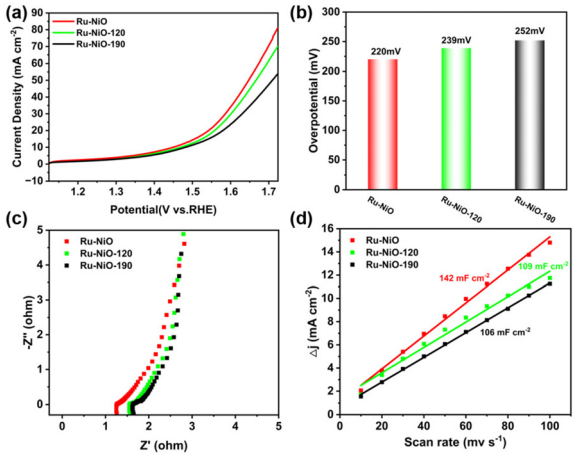

Fig. 4 (a) Polarization curves; (b) corresponding overpotential at 10 mA cm^{-2} (η_{10}); (c) Nyquist plots of Ru–NiO, Ru–NiO-120 and Ru–NiO-190 at a potential of 1.53 V (*vs.* RHE); (d) surface double-layer capacitance (C_{dl}) of Ru–NiO, Ru–NiO-120 and Ru–NiO-190.

In summary, based on the above-mentioned analysis, the formation mechanism of Ru–NiO by the different preparation methods is shown in Scheme 2, where the two-step thermal treatment method is more effective than the conventional sol–gel method and conventional calcination method in promoting the entry of the Ru atom into the NiO lattice. However, Ni^{2+} is reduced to metal Ni^0, leading to a phase change when the pretreatment temperature increase to 190 °C and higher, and a low deprotonation degrees occurs at a low temperature (120 °C). These results are disadvantageous for the formation of Ni/Ru–O–R or Ni[Ru(OR)$_{n+1}$], and further the generation of Ru–O–Ni bonds is difficult, ultimately making it challenging for the Ru atom to enter the NiO lattice. Briefly, an appropriate pretreatment temperature (160 °C) not only offers suitable conditions for the association reaction of bimetallic alcoholates, but also avoids the phase change caused by the reduction of polyhydric alcohol, finally resulting in the easier formation of Ru–O–Ni bonds and promoting the entry of the Ru atom into the NiO lattice.

3.3. DFT calculations for OER

DFT calculations were conducted to elucidate the intrinsic OER catalytic mechanism of Ru–NiO. Based on the four-step mechanism of adsorbate evolution under alkaline conditions, the optimal models (Ni atom in (200) crystal plane was chosen to adsorb O species in the pristine NiO and Ru–NiO models) and corresponding geometries of the various intermediates of Ru–NiO were established, as shown in Fig. 5a and Fig. S10a.† For comparison, that of pristine NiO was also calculated (Fig. 5b and Fig. S10b†). The Gibbs free energy can be obtained using the equation $G = E_H + E_{ZPE} - T_S$, where G stands for Gibbs free energy, and E_H, E_{ZPE} and T_S represent the total energy, zero-point energy and entropy of system, respectively. Generally, the step with the largest change in Gibbs free energy (ΔG) in the four-electron transfer step of alkaline OER is determined as the rate-determining step (RDS).[44] The rate-determining step (Max(ΔG), Fig. 5a and b) of pristine NiO and Ru–NiO is step one (Step I), which is homologous for them. It can also be concluded that the ΔG value of pristine NiO (ΔG_I = 1.55 eV) is greater than that of Ru–NiO (ΔG_I = 1.50 eV), which reveals that Ru–NiO needs a lower theoretical onset overpotential (0.27 V) for OER. This follows that the doping Ru atoms can induce lattice strain to optimize the adsorption energy of the oxygen-containing intermediates and reduce the reaction free energy barrier as well as accelerate the catalytic kinetics.[45] Furthermore, the electronic structures were calculated by using the VASP software based on the DFT+U method, aiming to gain a better understanding of the doping effect. The total density of states (TDOS) is plotted in Fig. 5c. It is seen that that doping with Ru atoms and introducing O vacancies can make the bandgap of NiO narrower, suggesting an improvement in its conductivity. In addition, the peak intensity of Ru–NiO is stronger than that of the pristine NiO near the Fermi level *via* the local amplification of TDOS, indicating its more conductive electronic structure (Fig. 5d).[46] As seen in Fig. 5e and f, the d-band center (ε_d) of Ru–NiO (ε_d = −1.78 eV) is closer to the Fermi level (E_0 = 0 eV) than that of the pristine NiO (ε_d = −2.89 eV). The upward shift in ε_d leads to an enhancement in the adsorption strength, making it easier for the OH reactant to be adsorbed and activated on the surface of the catalyst, thus improving the reactivity of the reaction.[47] These observations indicate that Ru doping primarily induces lattice strain, effectively optimizing the electronic structure of

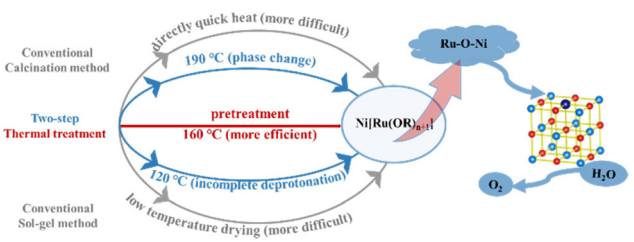

Scheme 2 Synthetic reaction mechanism of different methods for the substitution of Ru for Ni in the NiO lattice.

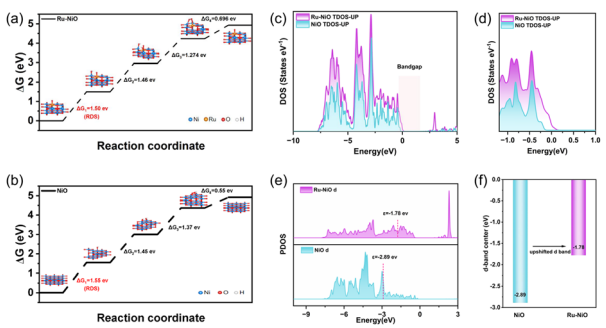

Fig. 5 (a and b) OER reaction mechanism diagram of Ru–NiO and NiO, and corresponding Gibbs free energy diagrams for both at U = 0 V; (c and d) total density of state (TDOS) curves of Ru–NiO and NiO; (e and f) Ni-projected DOS and calculated d-band center of Ru–NiO and NiO, respectively.

NiO, promoting the adsorption of the OER intermediates, and ultimately enhancing its OER performance. Hence, the theoretical analysis and experiment results are in excellent agreement on the fact that the OER performance of NiO can be regulated by Ru doping and introducing O vacancies. As listed in Table S6,† the surface oxygen vacancy formation energy of Ru–NiO is the smallest, indicating that oxygen vacancies are more likely to be formed after Ru doping into the NiO lattice. The Bader charge analysis revealed that the sectional charge of the Ni atom decreases from 1.2 to 1.16 when Ru is doped into the NiO lattice. On the one hand, it can be observed obviously that the electrons are withdrawn from the Ni atom to the Ru atom by the Ru–O–Ni bonds in Ru–NiO. On the other hand, the formation of oxygen vacancies can promote the formation of high-valence state Ni^{3+} active sites. These results are in accordance with the EIS and XPS results. In summary, the DFT calculations demonstrate that the lattice strain-induced surface structural distortion elevates the electronic state energy level, optimizing the adsorption of the intermediates, while increasing the population of Ni^{3+} active sites, thereby enhancing the OER performance.

4. Conclusion

In summary, we synthesized Ni^{3+}-rich, Ru-doped NiO nanoparticles (Ru–NiO) through a two-step thermal treatment method, which showed an excellent performance in the oxygen evolution reaction (OER). As an OER catalyst, the obtained Ru–NiO exhibited a low overpotential of 220 mV at the current density of 10 mA cm^{-2} and a Tafel slope of 78 mV dec^{-1} in alkaline media, outperforming most previously reported NiO-based electrocatalysts. Meanwhile, the superior OER performance of Ru–NiO is attributed to the lattice strain effect caused by the introduction of trace heterogeneous Ru atom. This result was further confirmed by the DFT results. Additionally, the experimental results suggest that using two-step thermal treatment method is easy to retain the Ru–O–Ni bond from the precursor, and furthermore form an Ni^{3+}-rich, Ru-doped NiO catalyst compared with the conventional sol–gel synthesis method and the conventional calcination synthesis method. We think that this study provides a simple and efficient improved sol–gel method for doping trace heterogeneous Ru atoms into the NiO lattice, which opens a new avenue for the design of nickel-based electrocatalysts with an enhanced OER catalytic performance.

Conflicts of interest

There are no conflicts to declare.

Data availability

All data generated or analyzed during this study are included in this published article and its ESI.†

Acknowledgements

This work is supported by the National Natural Science Foundation of China (Grant: 21771032).

References

1 Y. Li, Y. Sun, Y. Qin, W. Zhang, L. Wang, M. Luo, H. Yang and S. Guo, Recent Advances on Water-Splitting Electrocatalysis Mediated by Noble-Metal-Based Nanostructured Materials, *Adv. Energy Mater.*, 2020, **10**, 1903120.
2 Z. R. Shen, C. H. Xu, S. M. Wang, J. Chen, S. Q. Jia and Q. G. Wang, An active $ZnxNi_{1-x}S$@Mo_2C/carbon cloth electrode as efficient catalyst for water electrolysis, *Vacuum*, 2022, **196**, 110729.
3 J. Hou, Y. Wu, B. Zhang, S. Cao, Z. Li and L. Sun, Rational Design of Nanoarray Architectures for Electrocatalytic Water Splitting, *Adv. Funct. Mater.*, 2019, **29**, 1808367.
4 N. T. Suen, S. F. Hung, Q. Quan, N. Zhang, Y. J. Xu and H. M. Chen, Electrocatalysis for the oxygen evolution reaction: recent development and future perspectives, *Chem. Soc. Rev.*, 2017, **46**, 337–365.
5 F. Song, L. C. Bai, A. Moysiadou, S. Lee, C. Hu, L. Liardet and X. Hu, Transition metal oxides as electrocatalysts for the oxygen evolution reaction in alkaline solutions: an application-inspired renaissance, *J. Am. Chem. Soc.*, 2018, **140**, 7748–7759.
6 H. N. Nong, T. Reier, H.-S. Oh, M. Gliech, P. Paciok, T. H. T. Vu, D. Teschner, M. Heggen, V. Petkov, R. Schlögl, T. Jones and P. Strasser, A unique oxygen ligand environment facilitates water oxidation in hole-doped IrNiOx core-shell electrocatalysts, *Nat. Catal.*, 2018, **1**, 841–851.
7 J. Liu, Y. Zheng, Y. Jiao, Z. Wang, Z. Lu, A. Vasileff and S. Z. Qiao, NiO as a Bifunctional Promoter for RuO_2 toward Superior Overall Water Splitting, *Small*, 2018, **14**, 1704073.
8 Y. Li, J. Yin, Y. Feng, J. Li, H. Zhao, C. Zhu, D. Yue, Y. Liu, B. Su and X. Liu, Metal-organic Framework/Polyimide composite with enhanced breakdown strength for flexible capacitor, *Chem. Eng. J.*, 2022, **429**, 132228.
9 Q. R. Shi, C. Z. Zhu, D. Du and Y. H. Lin, Robust noble metal-based electrocatalysts for oxygen evolution reaction, *Chem. Soc. Rev.*, 2019, **48**, 3181–3192.
10 A. Roy, A. Ray, S. Saha, M. Ghosh, T. Das, B. Satpati, M. Nandi and S. Das, NiO-CNT composite for high performance supercapacitor electrode and oxygen evolution reaction, *Electrochim. Acta*, 2018, **283**, 327–337.
11 H. Wu, Y. Wang, C. Zheng, J. Zhu, G. Wu and X. Li, Multi-shelled NiO hollow spheres: easy hydrothermal synthesis and lithium storage performances, *J. Alloys Compd.*, 2016, **685**, 8–14.
12 P. Chaudhary and P. Ingole, *In situ* solid-state synthesis of 2D/2D interface between Ni/NiO hexagonal nanosheets supported on g-C_3N_4 for enhanced photo-electrochemical

water splitting, *Int. J. Hydrogen Energy*, 2020, **45**, 16060–16070.

13 D. J. Zhou, S. Y. Wang, Y. Jia, X. Y. Xiong, H. B. Yang, S. Liu, J. L. Tang, J. M. Zhang, D. Liu, L. R. Zheng, Y. Kuang, X. M. Sun and B. Liu, NiFe hydroxide lattice tensile strain: enhancement of adsorption of oxygenated intermediates for efficient water oxidation catalysis, *Angew. Chem., Int. Ed.*, 2019, **58**, 736–740.

14 T. Wu, M. Z. Sun and B. L. Huan, Strain modulation of phase transformation of noble metal nanomaterials, *InfoMat*, 2020, **2**, 715.

15 Z. Hou, C. Cui, Y. Li, Y. Gao, D. Zhu, Y. Gu, G. Pan, Y. Zhu and T. Zhang, Lattice-strain engineering for heterogenous electrocatalytic oxygen evolution reaction, *Adv. Mater.*, 2023, **35**, 2209876.

16 S. S. Xiong, S. T. Weng, Y. Tang, L. Qian, Y. Q. Xu, X. F. Li, H. J. Lin, Y. C. Xu, Y. Jiao and J. R. Chen, Mo-doped Co_3O_4 ultrathin nanosheet arrays anchored on nickel foam as a bi-functional electrode for supercapacitor and overall water splitting, *J. Colloid Interface Sci.*, 2021, **602**, 355–366.

17 H. M. Zhang, Y. Lv, C. Chen, C. W. Lv, X. Y. Wu, J. X. Guo and D. Z. Jia, Inter-doped ruthenium-nickel oxide heterostructure nanosheets with dual active centers for electrochemical-/solar-driven overall water splitting, *Appl. Catal., B*, 2021, **298**, 120611.

18 D. Mateos, B. Valdez, J. R. Castillo, N. Nedev, M. Curiel, O. Perez, A. Arias and H. Tiznado, Synthesis of high purity nickel oxide by a modified sol-gel method, *Ceram. Int.*, 2019, **45**, 11403–11407.

19 C. R. Michea, M. Mauricio, F. Gracia, G. Morell and E. Mosquera, Influence of copper doping on structural, morphological, optical, and vibrational properties of ZnO nanoparticles synthesized by sol gel method, *Surf. Interfaces*, 2020, **21**, 100700.

20 Y. Song, D. Feng, T. Liu, Y. Li and X. X. Liu, Controlled partial-exfoliation of graphite foil and integration with MnO_2 nanosheets for electrochemical capacitors, *Nanoscale*, 2015, **7**, 3581.

21 X. Zhang, X. Fang, K. Zhu, W. Yuan, T. Jiang, H. Xue and J. Tian, Fe-doping induced electronic structure reconstruction in Ni-based metal-organic framework for improved energy-saving hydrogen production via urea degradation, *J. Phys. Chem. Lett.*, 2022, **520**, 230882.

22 Y. Wang, Y. Xie, S. Yu, K. Yan, Y. Shao, L. Zou, B. Zhao, Z. Wang, Y. Ling and Y. Chen, Ni doping in unit cell of BiOBr to increase dipole moment and induce spin polarization for promoting CO_2 photoreduction via enhanced build-in electric field, *Appl. Catal., B*, 2023, **327**, 122420.

23 A. Laskavy, L. J. W. Shimon, L. Konstantinovski, M. A. Iron and R. Neumann, Activation of molecular oxygen by a dioxygenase pathway by a ruthenium bis-bipyridine compound with a proximal selenium site, *J. Am. Chem. Soc.*, 2010, **132**, 517–523.

24 X. D. Hao, A. Yoko, K. Inoue, Y. Xu, M. Saito and C. L. Chen, Atomistic origin of high-concentration Ce^{3+} in {100}-faceted Cr-substituted CeO_2 nanocrystals, *Acta Mater.*, 2021, **203**, 116473.

25 H. Yoon, H. J. Song, B. Ju and D. W. Kim, Cobalt phosphide nanoarrays with crystallineamorphous hybrid phase for hydrogen production in universal-pH, *Nano Res.*, 2020, **13**, 2469–2477.

26 Q. Hu, X. Huang, Z. Wang, G. Li, Z. Han, H. Yang, X. Ren, Q. Zhang, J. Liu and C. He, Unconventionally fabricating defect-rich NiO nanoparticles within ultrathin metal-organic framework nanosheets to enable high-output oxygen evolution, *J. Mater. Chem. A*, 2020, **8**, 2140.

27 G. Zhang, B. Wang, L. Li, S. Yang, J. Liu and S. Yang, Tailoring the electronic structure by constructing the heterointerface of RuO_2-NiO for overall water splitting with ultralow overpotential and extra-long lifetime, *J. Mater. Chem. A*, 2020, **8**, 18945.

28 X. Y. Chen, J. X. Song, Y. F. Xing, Y. Q. Qin, J. Lin, X. Qu, B. J. Sun, S. Y. Du, D. W. Shi, C. T. Chen and D. P. Sun, Nickel-decorated RuO_2 nanocrystals with rich oxygen vacancies for high-efficiency overall water splitting, *J. Colloid Interface Sci.*, 2023, **630**, 940–950.

29 J. Lee, S. H. Lee, Y. G. Kim, Y. J. Kwon, W. H. Kim, S. M. Chung, D. Kim and H. Kim, Atomic layer deposited RuO_2 with controlled crystallinity and thickness for oxygen evolution reaction catalysis, *Vacuum*, 2024, **220**, 112843.

30 X. Li, H. Zhang, Y. Liu, X. Duan, X. Xu, S. Liu, H. Sun and S. Wang, Synergy of NiO quantum dots and temperature on enhanced photocatalytic and thermophoto hydrogen evolution, *Chem. Eng. J.*, 2020, **390**, 124634.

31 T. Tang, W. J. Jiang, S. Niu, N. Liu, H. Luo, Q. Zhang, W. Wen, Y. Y. Chen, L. B. Huang, F. Gao and J. S. Hu, Kinetically controlled coprecipitation for general fast synthesis of sandwiched metal hydroxide nanosheets/graphene composites toward efficient water splitting, *Adv. Funct. Mater.*, 2020, **28**, 1704594.

32 H. Wang, Y. Wang, J. Zhang, X. Liu and S. Tao, Electronic structure engineering through Fe-doping CoP enables hydrogen evolution coupled with electro-Fenton, *Nano Energy*, 2021, **84**, 105943.

33 C. Yuan, S. Wang, K. Hui, K. Wang, J. Li, H. Gao, C. Zha, X. Zhang, D. A. Dinh, X. L. Wu, Z. Tang, J. Wan, Z. Shao and K. Hui, In situ immobilizing atomically dispersed Ru on oxygen-defective Co_3O_4 for efficient oxygen evolution, *ACS Catal.*, 2023, **13**, 2462–2471.

34 M. Xie, Y. Ma, D. Lin, C. Xu, F. Xie and W. Zeng, Bimetal-organic framework MIL-53 (Co-Fe): an efficient and robust electrocatalyst for the oxygen evolution reaction, *Nanoscale*, 2020, **12**, 67–71.

35 H. Y. Qin, G. L. Lin, J. Y. Zhang, X. J. Cao, W. Xia, H. C. Yang, K. N. Yuan, T. Jin, Q. L. Wang and L. F. Jiao, Enhanced Cooperative Generalized Compressive Strain and Electronic Structure Engineering in W-Ni_3N for Efficient Hydrazine Oxidation Facilitating H_2 Production, *Adv. Mater.*, 2025, **37**, 2417593.

36 T. Matsumoto, K. Takahashi, K. Kitagishi, K. Shinoda, J. L. C. Huaman, J.-Y. Piquemal and B. Jeyadevan,

Dissolution and reduction of cobalt ions in the polyol process using ethylene glycol: identification of the active species and its role, *New J. Chem.*, 2015, **39**, 5008–5018.

37 F. Bonet, C. Guéry, D. Guyomard, R. Herrera Urbina, K. Tekaia-Elhsissen and J.-M. Tarascon, Electrochemical reduction of noble metal compounds in ethylene glycol, *Int. J. Inorg. Mater.*, 1999, **1**, 47–51.

38 F. Bonet, C. Guéry, D. Guyomard, R. Herrera Urbina, K. Tekaia-Elhsissen and J.-M. Tarascon, Electrochemical reduction of noble metal species in ethylene glycol at platinum and glassy carbon rotating disk electrodes, *Solid State Ionics*, 1999, **126**, 337–348.

39 F. Jiang, G. Feng, C. J. Xu, S. Qing, Q. Wu, Y. Yu, Q. Zhang and W. H. Jiang, Novel facile nonhydrolytic sol-gel synthesis of $MgAl_2O_4$ nanocrystal from bimetallic alkoxides, *J. Sol-Gel Sci. Technol.*, 2021, **100**, 555–561.

40 P. H. Mutin and A. Vioux, Recent advances in the synthesis of inorganic materials via non-hydrolytic condensation and related low temperature routes, *J. Mater. Chem. A*, 2013, **1**, 11504.

41 J. Sun, Y. C. Liu, Y. D. Han, W. H. Li, N. Wang, L. Zhang, Y. Zhang, F. Y. Deng, D. S. Wang and X. Zhang, Enabling controllable time-dependent phosphorescence in carbonized polymer dots based on chromophore excited triplet energy level modulation by ionic bonding, *Angew. Chem., Int. Ed.*, 2025, **64**, e202415042.

42 J. Teichert, T. Doert and M. Ruck, Mechanisms of the polyol reduction of copper(II) salts depending on the anion type and diol chain length, *Dalton Trans.*, 2018, **47**, 14085–14093.

43 J. C. Yang and Y. G. Shul, Effects of ethylene glycol addition on the properties of Ru/Al_2O_3 catalyst prepared by sol-gel method, *Catal. Lett.*, 1996, **36**, 41–49.

44 L. Peng, J. Wang, Y. Nie, K. Xiong, Y. Wang, L. Zhang, K. Chen, W. Ding, L. Li and Z. Wei, Dual-ligand synergistic modulation: a satisfactory strategy for simultaneously improving the activity and stability of oxygen evolution electrocatalysts, *ACS Catal.*, 2017, **7**, 8184–8191.

45 X. Mu, H. Yuan, H. Jing, F. Xia, J. Wu, X. Gu, C. Chen, J. Bao, S. Liu and S. Mu, Superior electrochemical water oxidation in vacancy defect-rich 1.5 nm ultrathin trimetal-organic framework nanosheets, *Appl. Catal., B*, 2021, **296**, 120095.

46 W. D. Zhang, Q. T. Hu, L. L. Wang, J. Gao, H. Y. Zhu, X. Yan and Z. G. Gu, *In situ* generated Ni-MOF/LDH heterostructures with abundant phase interfaces for enhanced oxygen evolution reaction, *Appl. Catal., B*, 2021, **286**, 119906.

47 Z. L. Ju, X. Y. Zhang, Y. Wang, C. F. Yin and Q. X. Kang, B-doped CoN_4-Based catalysts as efficient Electrocatalysts for ORR/OER/HER with low overpotentials: Density functional theory studies, *Vacuum*, 2025, **233**, 114004.